J. Fluid Mech. (2008), *vol.* 605, *pp.* 227–252.
doi:10.1017/S0022112008001547 Printed in the United Kingdom

The effect of confinement on the stability of non-swirling round jet/wake flows

MATTHEW P. JUNIPER

Department of Engineering, University of Cambridge,
Trumpington Street, Cambridge, CB2 1PZ, UK

(Received 5 April 2007 and in revised form 12 March 2008)

It has recently been shown that the instability characteristics of planar jets and wakes change when the flows are confined between two flat plates. This is due to constructive interaction between modes with zero group velocity in the inner and outer flows. In this theoretical study, a linear spatio-temporal analysis is performed on unconfined and confined round jets and wakes in order to discover whether the same effect is observed. There are several similarities between the planar case and the round case as well as some significant differences. Nevertheless, the effect of confinement on round flows is found to be very similar to that on planar flows and to act via the same physical mechanism. This paper examines density ratios from 0.001 to 1000 and has important implications for the design of fuel injectors, which often employ confined shear flows at high Reynolds numbers and large density ratios to generate strong mixing in combustion chambers.

1. Introduction

This theoretical study examines the effect of confinement on the stability of non-swirling round jets and wakes. The results are compared with those of a similar study (Juniper 2006) on planar jets and wakes. These flows consist of a central fluid surrounded by an outer fluid, both of which are confined within a duct (figure 1). If the inner fluid moves faster than the outer fluid, it is a jet flow. If the outer fluid moves faster than the inner fluid, it is a wake flow.

Unconfined jets and wakes have already been extensively studied. Previous theoretical and experimental work on these configurations is reviewed by Huerre & Monkewitz (1990). The theoretical study of Monkewitz & Sohn (1988) and the experimental study of Sreenivasan *et al.* (1989) on low-density jets are particularly relevant to this paper. These flows behave as self-excited oscillators rather than as amplifiers of extrinsic perturbations, owing to a region of local absolute instability immediately downstream of the injection plane. By considering the effect of the shear-layer thickness and viscosity, Yu & Monkewitz (1990) concluded that the transition to absolute instability is caused by an interaction between the shear-layers on either side of the central fluid and is not a viscous effect. In this study, this interaction is examined when the flow is confined.

Confined jets and wakes have received less attention and their behaviour is less well understood. On the one hand, the experimental study of Shair *et al.* (1963) concluded that confinement stabilizes the flow around a cylinder at Reynolds numbers between 40 and 140. On the other hand, the experimental study of Bearman & Zdravkovich (1978) suggests that confinement increases the strength of absolute instability in a

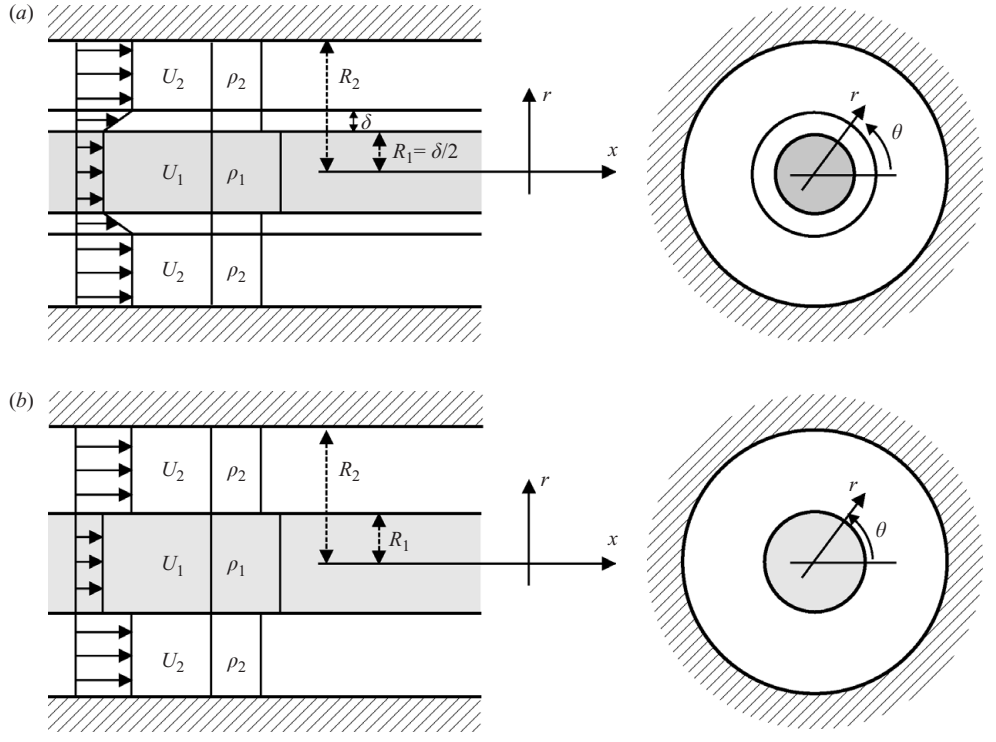

FIGURE 1. Two models are used in this paper. They consist of two coaxial inviscid incompressible flows confined within a duct. The first model has a piecewise linear velocity profile. The second model has a plug flow velocity profile.

similar flow at Reynolds numbers of 45 000. The theoretical study of Juniper & Candel (2003) has shown that planar inviscid jets and wakes become absolutely unstable over a wider range of shear when they are confined. The full background to this problem and its practical implications for fuel injection are explained in that paper and are not repeated here. The physical reason for this behaviour has been explained by Juniper (2006) for planar flows. In summary, when the flows have similar thicknesses, modes with zero group velocity in the inner flow interact with those in the outer flow. If these inner and outer modes have similar cross-stream wavenumbers, the flow is more unstable. If they have very different cross-stream wavenumbers, the flow is more stable. One aim of the present paper is to determine whether the same behaviour is found in confined round flows.

Curiously, some planar shear flows that are convectively unstable when unconfined become absolutely unstable when confined, even when the confining wall is placed far away from the shear layer. Healey (2007) found this behaviour in the rotating-disk boundary layer and showed that it is related to the convective instabilities with growth normal to the shear layer described in Healey (2006). Juniper (2006) found the same behaviour in planar jets and wakes and, in Juniper (2007), showed that it is due to the same type of instability as that in the rotating-disk boundary layer. A second aim of the present paper is to determine whether the same behaviour is found in non-swirling round jets and wakes.

In this study, a linear spatio-temporal stability analysis is used to determine the convective/absolute instability of confined jets and wakes as a function of shear,

density ratio, confinement and azimuthal wavenumber. Linear analyses are very successful at predicting the onset of global modes, for reasons described in Delbende & Chomaz (1998), so a nonlinear analysis is not attempted. Contours of angular frequency, ω, are plotted in the wavenumber, k, plane to reveal the saddle points of $\omega(k)$, which determine the long-time behaviour of the flow. By studying the positions of these saddle points as the confinement changes, the effect of confinement is explained physically.

In §2, the round models are described in more detail and the unconfined and confined dispersion relations are derived for normal mode perturbations. These are shown to be equivalent to those of the planar model in the limit of small curvature. In §3, the full impulse response in the outer flow is evaluated and the physical origins of each saddle point are identified. The effect of the shear-layer thickness on unconfined jets and wakes is examined in §4 and the effect of the density ratio is studied in §5 over a higher range of density ratios than in previous studies. The effect of confinement on uniform density jets and wakes is examined in §6 and explained in terms of the interaction between the modes with zero group velocity in the inner and outer flows. Finally, the effect of confinement on non-uniform density jets and wakes is examined in §7.

2. The models and their dispersion relations

Two models are used in this paper. Both are axisymmetric and assume inviscid, incompressible flows. The first model, figure 1(*a*), has a piece-wise linear velocity profile between an inner flow with velocity U_1 and density ρ_1 and an outer flow with velocity U_2 and density ρ_2. The shear-layer extends from $R_1 - \delta/2$ to $R_1 + \delta/2$ and is located entirely in the outer flow. The outer flow has radius R_2, which can extend to infinity. The second model has a plug flow velocity profile with an infinitely thin shear layer. Both models have infinite extent in the x-direction.

2.1. *Analysis common to both models*

The models assume a base flow $U(r)$ and normal mode decompositions for the perturbation fields: pressure, $p(r)\exp\{\mathrm{i}(kx+m\theta-\omega t)\}$; axial velocity, $u(r)\exp\{\mathrm{i}(kx+m\theta-\omega t)\}$; radial velocity, $v(r)\exp\{\mathrm{i}(kx+m\theta-\omega t)\}$ and azimuthal velocity, $w(r)\exp\{\mathrm{i}(kx+m\theta-\omega t)\}$. These are substituted into the linearized Euler equations to give the governing equations:

$$\mathrm{i}ku\,(U-c)+vU'=-\frac{1}{\rho}\mathrm{i}kp, \tag{2.1}$$

$$\mathrm{i}kv\,(U-c)=-\frac{1}{\rho}p', \tag{2.2}$$

$$\mathrm{i}kw\,(U-c)=-\frac{\mathrm{i}}{\rho}\frac{m}{r}p, \tag{2.3}$$

$$\mathrm{i}ku+v'+\frac{v}{r}+\frac{\mathrm{i}}{r}mw=0, \tag{2.4}$$

where $c\equiv\omega/k$ and prime denotes $\mathrm{d}/\mathrm{d}r$. These four ODEs in four unknown functions can be reduced to one ODE in one unknown function, for example the pressure perturbation:

$$[r^2p''+rp'-(k^2r^2+m^2)p]\,(U-c)-2r^2U'p'=0. \tag{2.5}$$

In general, (2.5) has no analytical solution. In the inner and outer fluids, however, where $U' = 0$, (2.5) reduces to the modified Bessel equation, (2.6), provided that $U \neq c$, which is always satisfied for complex c:

$$r^2 p'' + rp' - (k^2 r^2 + m^2)p = 0. \tag{2.6}$$

Equation (2.6) has general solution

$$p(r;k) = A_i \mathrm{I}_m(\xi r) + B_i \mathrm{K}_m(\xi r), \tag{2.7}$$

where I_m and K_m are modified Bessel functions, m is the azimuthal wavenumber of each normal mode and $\xi \equiv +\sqrt{k^2}$. In this paper, index i is 1 for the inner fluid and 2 for the outer fluid.

In the inner fluid, $B_1 = 0$ because K_m tends to infinity as ξr tends to zero. In the outer fluid, if the flow is unconfined, $A_2 = 0$ because I_m tends to infinity as ξr tends to infinity. If the flow is confined, however, the boundary condition of zero r-velocity at $r = R_2$ fixes $A_2/B_2 = -\mathrm{K}'_m(\xi R_2)/\mathrm{I}'_m(\xi R_2)$. Therefore, the pressure perturbations are:

$$p_1(r;k) = A_1 \mathrm{I}_m(\xi r), \tag{2.8}$$

$$p_2(r;k) = B_2 \mathrm{K}_m(\xi r) \quad \text{when unconfined}, \tag{2.9}$$

$$p_2(r;k) = \overline{B}_2 \{\mathrm{I}_m(\xi r)\mathrm{K}'_m(\xi R_2) - \mathrm{K}_m(\xi r)\mathrm{I}'_m(\xi R_2)\} \quad \text{when confined}. \tag{2.10}$$

Choosing ξ as the positive root of k^2 ensures that the argument of the Bessel functions is always positive. This is required when the flow is unconfined because p_2 in (2.9) must tend to zero as r tends to infinity. It is not strictly required when the flow is confined, however, because p_2 in (2.10) is invariant under the transformation $\xi \leftrightarrow -\xi$. Consequently, equations that relate to the confined case are unchanged if ξ is replaced with k.

There is one kinematic and one dynamic matching condition at each fluid interface:

$$\Delta \left[\frac{p'}{\rho (U-c)^2} \right] = 0, \tag{2.11}$$

$$\Delta p = 0. \tag{2.12}$$

It remains to apply these matching conditions between the fluids, which is where the models differ.

2.2. *Analysis specific to the piece-wise linear velocity profile*

In the piece-wise linear model, there are no velocity discontinuities at the fluid interfaces so the matching conditions reduce to:

$$\frac{p'}{\rho_2} = \frac{p'_1}{\rho_1}, \quad p = p_1 \quad \text{at } r = R_1 - \delta/2, \tag{2.13}$$

$$p' = p'_2, \quad p = p_2 \quad \text{at } r = R_1 + \delta/2\ , \tag{2.14}$$

where p without a subscript is the pressure perturbation within the shear layer. By substituting from (2.8), (2.9) and (2.10), these matching conditions can be expressed as:

$$\frac{p'}{p} = k \frac{\rho_2}{\rho_1} \frac{\mathrm{I}'_m(\xi(R_1 - \delta/2))}{\mathrm{I}_m(\xi(R_1 - \delta/2))}, \tag{2.15}$$

at $R_1 - \delta/2$, and one of the following expressions at $R_1 + \delta/2$:

$$\frac{p'}{p} = \xi \frac{\mathrm{K}'_m(\xi(R_1 + \delta/2))}{\mathrm{K}_m(\xi(R_1 + \delta/2))} \quad \text{when unconfined}, \tag{2.16}$$

$$\frac{p'}{p} = \xi \frac{\mathrm{I}'_m(\xi(R_1+\delta/2))\mathrm{K}'_m(\xi R_2) - \mathrm{K}'_m(\xi(R_1+\delta/2))\mathrm{I}'_m(\xi R_2)}{\mathrm{I}_m(\xi(R_1+\delta/2))\mathrm{K}'_m(\xi R_2) - \mathrm{K}_m(\xi(R_1+\delta/2))\mathrm{I}'_m(\xi R_2)} \quad \text{when confined.} \tag{2.17}$$

Equation (2.5) is then solved numerically subject to boundary condition (2.15) and either (2.16) if unconfined or (2.17) if confined. This eigenvalue problem can be expressed as:

$$\mathrm{X}\tilde{p} = c\mathrm{Y}\tilde{p}, \tag{2.18}$$

where $\tilde{p}$ is a vector of the pressure values at N Chebyshev-spaced points between $R_1 - \delta/2$ and $R_1 + \delta/2$. Matrices X and Y represent the operations:

$$\mathrm{X} = Ur^2\frac{\mathrm{d}^2}{\mathrm{d}r^2} + Ur\frac{\mathrm{d}}{\mathrm{d}r} - U(k^2r^2+m^2) - 2r^2U'\frac{\mathrm{d}}{\mathrm{d}r}, \tag{2.19}$$

$$\mathrm{Y} = r^2\frac{\mathrm{d}^2}{\mathrm{d}r^2} + r\frac{\mathrm{d}}{\mathrm{d}r} - (k^2r^2+m^2), \tag{2.20}$$

and (2.18) can also be expressed as:

$$D(k,\omega) \equiv \det|\mathrm{X} - c\mathrm{Y}| = 0. \tag{2.21}$$

The top and bottom rows of X and Y, which correspond to the points $r = R_1 - \delta/2$ and $r = R_1 + \delta/2$ are replaced by boundary conditions (2.15) and either (2.16) or (2.17). The matrix eigenvalue problem is solved using Matlab's `eig` function. For each value of k, there are two physically relevant eigenvalues for ω. In this paper, N is usually 21, although this is increased around the branch cut near the k_r-axis in figure 2.

2.3. *Analysis specific to the plug flow velocity profile*

In the plug flow model, the inner and outer fluids can be matched directly with (2.11) and (2.12). This leads to the analytic dispersion relation:

$$D(k,\omega) \equiv A_2D^- + B_2D^+ = 0, \tag{2.22}$$

where
$$D^- \equiv \rho_1(U_1-c)^2\mathrm{I}_m(\xi r)\mathrm{I}'_m(\xi r) - \rho_2(U_2-c)^2\mathrm{I}_m(\xi r)\mathrm{I}'_m(\xi r), \tag{2.23}$$

and
$$D^+ \equiv \rho_1(U_1-c)^2\mathrm{I}_m(\xi r)\mathrm{K}'_m(\xi r) - \rho_2(U_2-c)^2\mathrm{K}_m(\xi r)\mathrm{I}'_m(\xi r). \tag{2.24}$$

The boundary condition on the outer flow yields either $A_2 = 0$ if the outer flow is unconfined, or $A_2/B_2 = -\mathrm{K}'_m(\xi R_2)/\mathrm{I}'_m(\xi R_2)$ if it is confined. For each value of k, there are two eigenvalues for ω, which are the same as those found for the piece-wise linear profile in the limit $\delta \to 0$.

2.4. *Non-dimensionalization*

It is convenient to introduce a non-dimensional framework and the following reference scales: velocity, $U_{ref} \equiv (U_1+U_2)/2$; length, R_1; density, ρ_2. The dimensionless variables are $\omega^* \equiv \omega R_1/U_{ref}$ and $k^* \equiv kR_1$. The dimensionless parameters are $\Lambda \equiv (U_1 - U_2)/(U_1+U_2)$, $S \equiv \rho_1/\rho_2$ and $R \equiv R_2/R_1$. The dispersion relations for unconfined and confined perturbations of the plug flow model are, respectively,

$$D^* \equiv S\frac{(1+\Lambda-c^*)^2}{(1-\Lambda-c^*)^2} - \frac{\mathrm{K}_m(\xi^*)\mathrm{I}'_m(\xi^*)}{\mathrm{I}_m(\xi^*)\mathrm{K}'_m(\xi^*)} = 0, \tag{2.25}$$

$$D^* \equiv S\frac{(1+\Lambda-c^*)^2}{(1-\Lambda-c^*)^2} - \frac{\mathrm{I}'_m(\xi^*)\left(\mathrm{I}_m(\xi^*)\mathrm{K}'_m(\xi^*R) - \mathrm{K}_m(\xi^*)\mathrm{I}'_m(\xi^*R)\right)}{\mathrm{I}_m(\xi^*)\left(\mathrm{I}'_m(\xi^*)\mathrm{K}'_m(\xi^*R) - \mathrm{K}'_m(\xi^*)\mathrm{I}'_m(\xi^*R)\right)} = 0. \tag{2.26}$$

In the rest of this paper the non-dimensional framework will be used and the asterisks will be dropped. It is conventional to use Λ as the shear parameter. However, the parameter $1/\Lambda$ is used for figures in this paper because this allows absolutely unstable regions to be plotted as single regions in parameter space. In the planar problem, the confinement, h, is defined as the ratio of the thickness of the outer flow to half the thickness of the inner flow. Its counterpart in the round case is $(R_2 - R_1)/R_1$, which is $R - 1$ in non-dimensional terms. This is also given the symbol h.

2.5. *Limits of negligible curvature*

If the azimuthal curvature is negligible relative to the axial curvature, then the dispersion relations are the same as the planar dispersion relations found in Juniper (2006). When $\xi \gg |m^2 - 1/4|$, the modified Bessel functions are approximately:

$$\mathrm{I}_m(\xi) \approx \sqrt{\frac{1}{2\pi\xi}}\mathrm{e}^{\xi}, \tag{2.27}$$

$$\mathrm{K}_m(\xi) \approx \sqrt{\frac{\pi}{2\xi}}\mathrm{e}^{-\xi}, \tag{2.28}$$

$$\mathrm{I}'_m(\xi) \approx \sqrt{\frac{1}{2\pi\xi}}\mathrm{e}^{\xi}, \tag{2.29}$$

$$\mathrm{K}'_m(\xi) \approx -\sqrt{\frac{\pi}{2\xi}}\mathrm{e}^{-\xi}. \tag{2.30}$$

Substituting into (2.25) and (2.26) gives

$$D \equiv S\frac{(1+\Lambda-c)^2}{(1-\Lambda-c)^2} + 1 = 0 \quad \text{when unconfined,} \tag{2.31}$$

$$D \equiv S\frac{(1+\Lambda-c)^2}{(1-\Lambda-c)^2} + \coth(\xi h) = 0 \quad \text{when confined.} \tag{2.32}$$

In this limit, the unconfined round shear layer behaves like an unconfined planar single shear layer. Similarly, the confined round shear layer behaves like a single planar shear layer placed a distance h from a wall, which in turn behaves like a varicose unconfined double shear layer of width $2h$ when the image shear layer is taken into account. In this paper, the azimuthal curvature is negligible only in the strongly confined case or at large radii.

2.6. *Integration in the plane of diverging eigenfunctions*

This section briefly summarizes integration in the plane of diverging eigenfunctions. More detail can be found in Healey (2007) and Juniper (2007).

In the complex k-plane, the function ξ has branch cuts up and down the k_i-axis, with branch points at $\pm\epsilon\mathrm{i}$, where $\epsilon \to 0$. In the unconfined case, the boundary condition (2.16) and the dispersion relation (2.25) are non-analytic at these branch cuts. These branch cuts therefore persist when contours of ω_i are plotted in the k-plane for the unconfined case. In the confined case, however, the combined boundary conditions (2.15) and (2.17), as well as the dispersion relation (2.26), are invariant under the transformation $\xi \leftrightarrow -\xi$. This means that these functions are analytic at these branch cuts and therefore that these branch cuts are absent when contours of ω_i are plotted in the k-plane for the confined case.

The branch cuts that arise in the unconfined case are then dealt with as follows. In §3, the impulse response is evaluated by integrating solutions of the dispersion relation

from $k = -\infty$ to $k = +\infty$. The integration path is deformed from the real k-axis and it is possible to evaluate the integral entirely on the plane of converging eigenfunctions, which is where $\mathrm{Re}\{\xi\} > 0$. The integral is sometimes easier to evaluate, however, by shifting the branch cut off the k_i-axis and integrating over a small region in the plane of diverging eigenfunctions, where $\mathrm{Re}\{\xi\} < 0$. It is important to point out that this is not the plane of diverging eigenfunctions that was rejected when A_2 was set to zero between (2.7) and (2.9); along the integration path, A_2 remains zero and the dispersion relation remains $D = D^+$ in (2.24). In the plane of diverging eigenfunctions, saddle points that lie on the integration path correspond to areas of the wavepacket that are growing in the cross-stream direction. In other words, for that area of the wavepacket, the growth rate along a ray at slightly larger r/t is greater than that along a ray at sightly smaller r/t. These areas are permissible because they are localized within the wavepacket and, at high r/t, all eigenfunctions become convergent.

3. Spatio-temporal stability analysis

The analysis in this section closely follows that in §3 of Juniper (2007) so that the round case studied in this paper can be compared directly with the planar case studied in that paper. In particular, figures 2 and 3 are at the same parameter values as figures 3 and 4 of Juniper (2007).

3.1. *Development of an expression for the full impulse response*

Each mode of the pressure perturbation is of the form $P(x, r, \theta, t) = p(r; k)\exp\{\mathrm{i}(kx + m\theta - \omega t)\}$, where $p(r; k)$ is given by (2.8) to (2.10) within fluids 1 and 2 and by the relevant eigenfunction of (2.18) within the shear layer. The impulse response is evaluated in the (x, r)-plane at $\theta = 0$ and the θ-dependence can be inferred from the azimuthal wavenumber, m, which from now on is treated as another parameter in the model. The pressure perturbation is expressed as the double Fourier integral of its normal mode perturbations, with the r-dependence included:

$$P(x, r, t) = \frac{1}{(2\pi)^2}\int_{F_k}\int_{L_\omega} \hat{p}(k, \omega)p(r; k)\mathrm{e}^{\mathrm{i}(kx-\omega t)}\mathrm{d}\omega\,\mathrm{d}k. \tag{3.1}$$

The dispersion relation $D(k, \omega)$ can be associated with a differential operator $D(-\mathrm{i}\partial/\partial x, \mathrm{i}\partial/\partial t)$ that relates the pressure perturbation $P(x, r, t)$ to a forcing $S(x, r, t)$ by $DP(x, r, t) = S(x, r, t)$, as in Huerre (2000). If the forcing is an impulse that excites all modes equally at $(x, t) = (0, 0)$ then $S(x, r, t)$ takes the form:

$$S(x, r, t) = \frac{1}{(2\pi)^2}\int_{F_k}\int_{L_\omega} \hat{S}(k, \omega)p(r; k)\mathrm{e}^{\mathrm{i}(kx-\omega t)}\mathrm{d}\omega\,\mathrm{d}k, \tag{3.2}$$

where $\hat{S}(k, \omega) = 1$. Although this impulse is not localized, the response is the same as that from a point impulse on the shear layer, as shown for the planar case in Juniper (2007). By substitution, the equation of motion in spectral space is then simply $\hat{p}(k, \omega)D(k, \omega) = \hat{S}(k, \omega) = 1$.

The integral in ω is evaluated with the residue theorem. For each value of k, two values of ω satisfy $D(k, \omega) = 0$ so there are two separate integrals of the form:

$$P(x, r, t) = -\frac{\mathrm{i}}{2\pi}\int_{F_k} \frac{p_i(r; k)}{\partial D/\partial\omega[k, \omega(k)]}\mathrm{e}^{-\mathrm{i}(\omega-kx/t)t}\mathrm{d}k. \tag{3.3}$$

In a conventional spatio-temporal stability analysis, $p_i(r; k)$ is dropped and (3.3) is evaluated in the long-time limit at $x/t = 0$. This type of analysis is used in §§4 to 7.

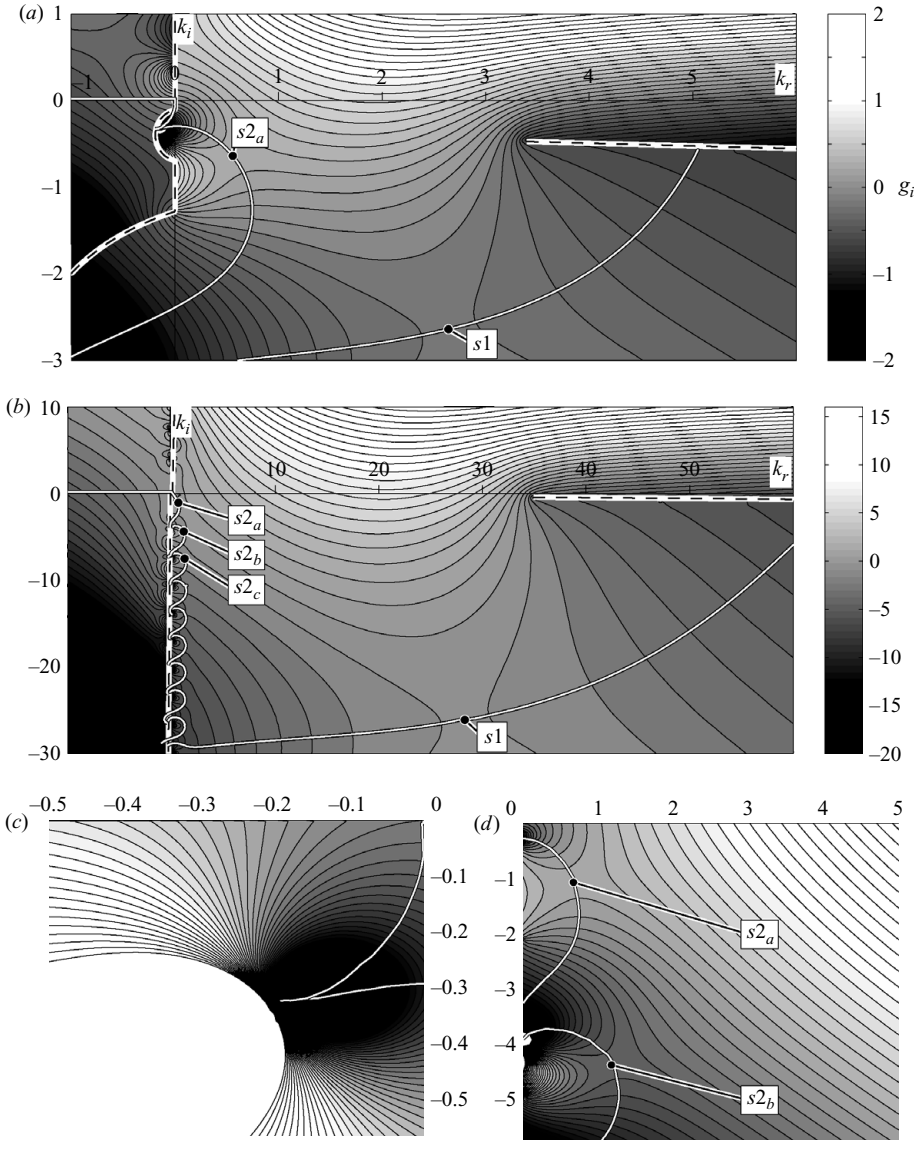

FIGURE 2. Contours of the growth rate, g_i, in the complex k-plane along the ray $(x/t, r/t) = (0.2, 0.1)$ for $m = 0$ perturbations of the piecewise linear model with $(1/\Lambda, S) = (1.1, 0.1)$ and shear-layer thickness (*a*) $\delta = 0.5$ and (*b*) $\delta = 0.05$. The integration path (white line) passes over saddle $s1$ and one or more of the $s2$ saddles. Branch cuts are shown as dotted lines. In (*a*) the branch cut has been shifted off the k_i-axis to reveal the integration path in the plane of diverging eigenfunctions. The top part of this is magnified in (*c*) to show how the integration path passes via a well in this plane. (*d*) shows a magnification of (*b*) around the top two saddle points, where it can be seen that $s2_a$ is higher than $s2_b$.

For both unconfined and confined flows, the response can also be evaluated easily along rays $x/t =$ constant. When the flow is unconfined, however, a further analysis is possible in which the impulse response is evaluated along rays of constant $(x/t, r/t)$ in the entire outer fluid, as in Healey (2006) for the rotating-disk boundary layer and

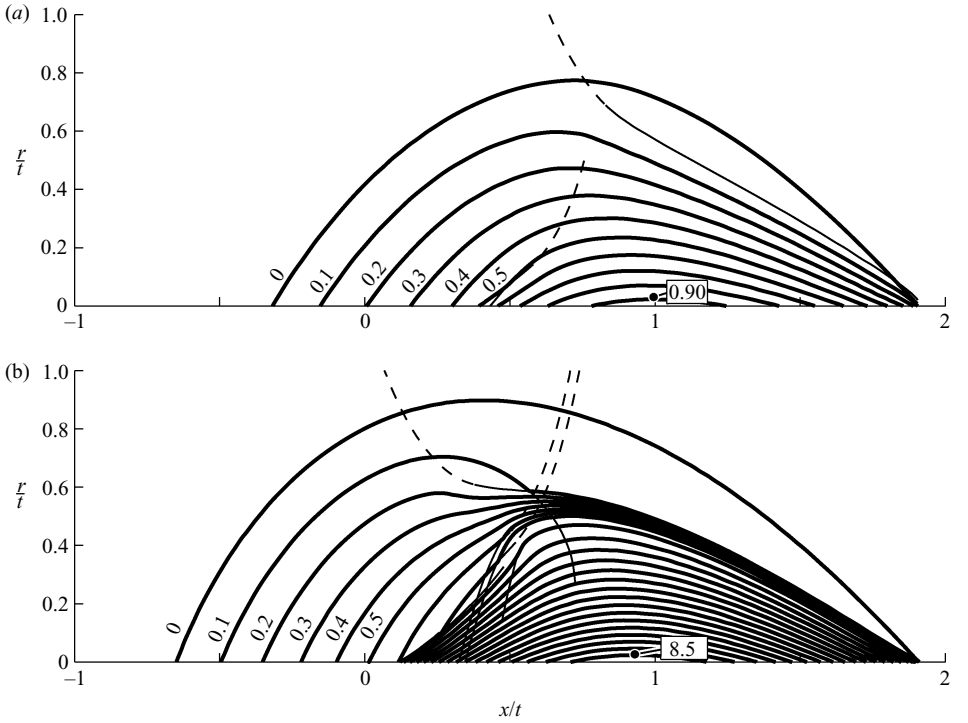

FIGURE 3. Contours of the growth rate, g_i, in the $(x/t, r/t)$-plane for the same parameter values as figure 2 with (*a*) $\delta = 0.5$ and (*b*) $\delta = 0.05$. The dominant saddle point is shown as a thick solid line, subdominant saddles as thin solid lines and saddle points that have moved off the integration path are thin dashed lines. The $s1$ saddle dominates at the centre of the wavepacket. It has the highest growth rate, but is not absolutely unstable. The $s2$ saddle dominates at the back of the wavepacket and is absolutely unstable.

Juniper (2007) for jets and wakes. All three analyses use the same technique, which is described in the next section.

3.2. *Evaluation of the impulse response in the entire outer fluid*

Equation (3.3) is usually evaluated in the long-time limit. If it is evaluated on rays of constant r/t at large times then r is also large. In the limit of large kr, the eigenfunction in the outer fluid (2.9) can be simplified by substituting (2.28). The eigenfunction $p(r;k)$ can then be absorbed into the exponential in the integrand of (3.3):

$$P(x,r,t) = -\frac{\mathrm{i}}{2\pi}\int_{F_k} \frac{B_2}{\partial D/\partial\omega[k,\omega(k)]}\sqrt{\frac{\pi}{2\xi r}}\mathrm{e}^{-\mathrm{i}g(k)t}\,\mathrm{d}k$$
$$\text{where } g(k) \equiv \{\omega(k) - \mathrm{i}\xi r/t - kx/t\}. \tag{3.4}$$

This is evaluated in the complex k-plane from $k = -\infty$ to $k = +\infty$. The integration path is shifted from the positive k_r-axis, without passing over any poles or branch points of $g(k)$, such that the maximum value of g_i along the whole path is as low as possible. In the long-time limit, the integral is dominated by the contribution from this maximum value of g_i. The path follows lines of constant g_r so that all contributions to the integral have the same phase (i.e. to avoid oscillations due to the $\exp(-\mathrm{i}g_r)$ term). The manifold $g(k)$ is hyperbolic everywhere so these maxima of g_i

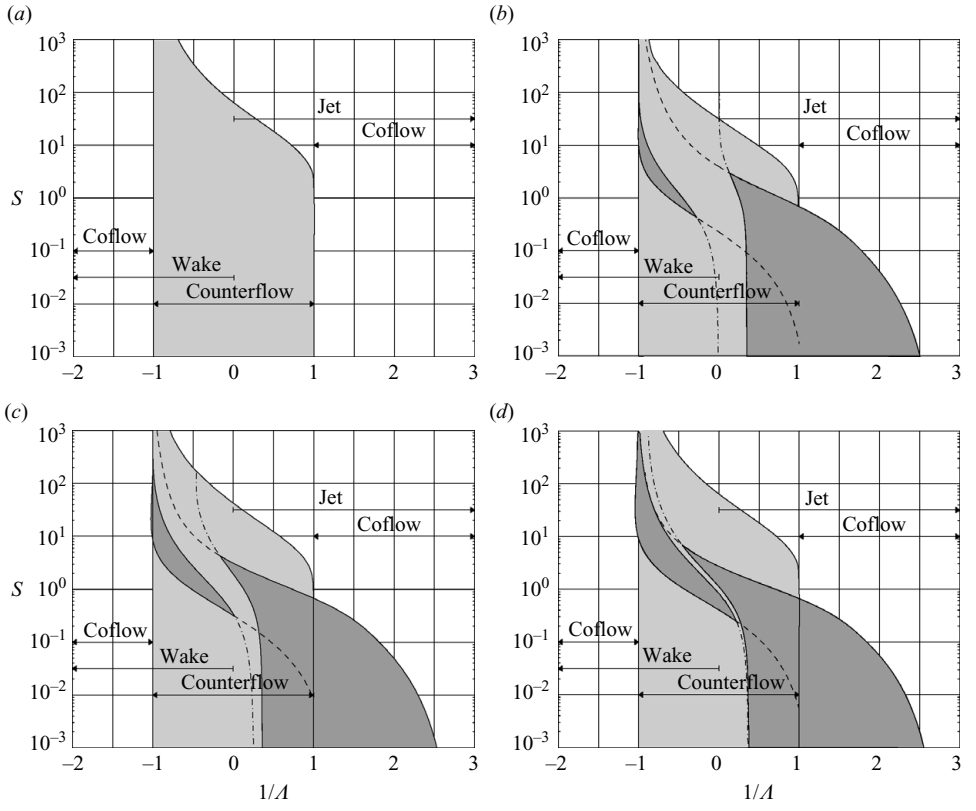

FIGURE 4. Absolutely unstable regions as a function of shear, Λ, and density ratio, S, for (a) a single shear layer, (b) $m = 0$ perturbations with $\delta = 0.1$, (c) $m = 0$ with $\delta = 0.05$ and (d) $m = 0$ with $\delta = 0.01$. The absolutely unstable region of the $s1$ saddle is light grey and that of the $s2_a$ saddle is dark grey. The boundaries of the $s2_a$ region are continued on one side by the dashed line, which shows the boundary where the $s2_a$ saddle becomes absolutely unstable, and on the other side by the dot-dashed line, which shows the boundary where the $s2_a$ saddle moves off the integration path.

are saddle points of $g(k)$. In general, saddle points do not have the same value of g_r, so the paths over adjacent saddles are joined at strongly negative values of g_i, where the contribution to the integral is negligible.

For instance, contours of g_i in the k-plane are shown in figure 2(a) for the $m = 0$ perturbation with $(1/\Lambda, S, \delta) = (1.1, 0.1, 0.5)$ and $(x/t, r/t) = (0.2, 0.1)$. The integration path passes between two branch points either side of $k = 0$, into a trough around $k = -0.12 - 0.32\mathrm{i}$, over saddle point $s2_a$, into another trough at the bottom left of the figure, over saddle point $s1$, into another trough that lies through the branch cut near the real axis, back round the branch point at $k = 3.42 - 0.45\mathrm{i}$ and eventually back onto the k_r-axis as $k_r \to \infty$ (not shown). In this figure, the branch cut has been shifted off the k_i-axis, as described in §2.6, so that the path can pass through a small region of the plane of diverging eigenfunctions.

For comparison, the same situation is shown in figure 2(b) with a shear-layer that is ten times thinner. Note that the axes have been scaled up by a factor of ten. The integration path now passes over a family of $s2$ saddle points before passing over the $s1$ saddle point and following a similar path to the previous case. As δ decreases

further, saddle $s1$ moves to higher k_r and the integration path passes over more of the $s2$ saddles. Consequently, the position of saddle $s1$ dictates which of the $s2$ saddles lie on the integration path. In figures 2(*a*) and 2(*b*), the dominant contribution in the long-time limit comes from saddle $s2_a$ because it is the highest point along the integration path. However, saddle $s1$ dominates at some other parameter values and on other rays $(x/t, r/t)$.

In figure 3, contours of the growth rates of the $s1$ and $s2_a$ saddles are shown in the $(x/t, r/t)$-plane for the same parameter values as figures 2(*a*) and 2(*b*). For each contour, the dominant saddle point is shown as a thick solid line, subdominant saddles are shown as thin solid lines and saddles that have moved off the integration contour are shown as thin dashed lines. The flow is dispersive, so the different Fourier components of the response travel at different group velocities, $(x/t, r/t)$, and are eventually found at different places. As for the planar case in Juniper (2007), the $s1$ saddle dominates around the centre of the wavepacket and the $s2_a$ saddle dominates at the back of the wavepacket.

Physically, saddle $s1$ is associated with the instability of the shear layer and has a wavelength that scales with the thickness of the shear layer. The $s2$ saddles are associated with the motion of the entire flow, which is the longer wavelength axisymmetric bulging for $m = 0$, helical spiralling for $m = 1$, double-helical spiralling for $m = 2$ etc. In counter-flow, when $|1/\Lambda| < 1$, the $s1$ saddle usually dominates at the point of impulse and causes the flow to be absolutely unstable. This is detailed in §4. In co-flow, when $|1/\Lambda| > 1$, the $s1$ saddle point is never absolutely unstable, but the $s2$ saddle points can be.

Examination of the full impulse response in the outer fluid reveals whether or not there are perturbations that grow in the cross-stream direction, which are associated with saddle points that cross the k_i-axis. These cause some flows that would be convectively unstable when unconfined, to be absolutely unstable when confined by a distant boundary. In the non-swirling round case studied in this paper, the dominant saddle point never crosses the k_i-axis (although some subdominant saddles do). This means that the wavepacket always decays in the cross-stream direction and therefore that a flow that is convectively unstable when unconfined remains convectively unstable when confined by a distant boundary. Having used the full impulse response in the outer fluid to confirm this, a conventional spatio-temporal stability analysis is used in the rest of this paper. It is worth noting that the approximation (2.28) is required only when calculating the response in the outer fluid. It is not required for the conventional analysis in the rest of this paper.

4. Effect of the shear-layer thickness

As the shear-layer thickness decreases, saddle $s1$ moves to higher k_r and the $s2$ saddles stay in the same places. It is useful to trace out the absolutely unstable region that is caused by the shear layer alone (i.e. saddle $s1$) in the limit $\delta \to 0$. In this limit, saddle $s1$ is no longer affected by the curvature of the shear layer and therefore its position can be found with a planar analysis. The region of absolute instability of this saddle as a function of shear and density ratio is shown in figure 4(*a*). The most important point to note is that the $s1$ saddle point is never absolutely unstable in co-flow. A secondary point is that, because the shear layer is located entirely in fluid 2, the absolutely unstable region is not symmetric under the transformation $(\rho_1, U_1) \leftrightarrow (\rho_2, U_2)$, which in non-dimensional terms is $(1/\Lambda, S) \leftrightarrow (-1/\Lambda, 1/S)$.

The position of saddle $s1$ determines whether or not the $s2_a$ saddle point lies on the integration path. If saddle $s2_a$ lies on the path and has positive growth rate, then the flow is absolutely unstable to the $s2_a$ saddle. Figures 4(b) to 4(d) show the absolutely unstable regions of both the $s1$ (light grey) and $s2_a$ (dark grey) saddles for the $m = 0$ mode of round jets/wakes at shear-layer thicknesses (b) $\delta = 0.1$, (c) $\delta = 0.05$ and (d) $\delta = 0.01$. In the area between the two dark grey regions, the integration path passes only over the s_1 saddle point, so the $s2_a$ saddle does not lie on the path. This area shrinks as the shear-layer thickness decreases and the absolutely unstable regions of the $s2_a$ saddles nearly join up. The absolutely unstable regions due to the other $s2$ saddles ($s2_b, s2_c, \ldots$) occur within that of the $s2_a$ saddle and are not shown here.

The positions of the $s2$ saddles, which are associated with the confined jet/wake behaviour, depend on the configuration: they differ between planar and round flows, between jets and wakes, and between confined and unconfined flows. The position of the $s1$ saddle, which is associated with the shear layer, is the same in all configurations when the shear layer is thin. This paper is concerned with the effect of confinement and therefore with the $s2$ saddles. Apart from the saddle selection described in the previous paragraph, there is little interaction between the $s1$ and $s2$ saddle points when the shear layer is very thin. In the rest of this paper, the $s1$ and $s2$ saddle points are considered separately. The absolutely unstable region due to the $s1$ saddle is calculated with the planar model of Juniper (2007) and the absolutely unstable region due to the $s2_a$ saddle is calculated with the analytic dispersion relation derived from the plug flow model shown in figure 1(b). The piece-wise linear model in figure 1(a) is used to determine whether or not the $s2$ saddle points found with the plug flow model lie on the integration path. This reduces computational time without loss of accuracy. In this approximation, figure 4(d) becomes figure 6(c).

5. Effect of shear and density ratio on unconfined jets and wakes

The positions of the $s2$ saddle points for varicose and sinuous motions of a planar jet are compared with those of the $m = 0$ and $m = 1$ motions of a round jet in figure 5. It was shown in § 2 that the combination of Bessel functions found in the dispersion relation (2.26) tends to $\coth(kh)$ for large k and therefore that the round case behaves like the planar case in this limit. Figure 5 shows that the manifolds and mode shapes of the planar varicose case (figure 5a) and the round $m = 0$ case (figure 5c) are broadly similar. Likewise, those of the planar sinuous case (figure 5b) and the helical $m = 1$ case (figure 5d) are broadly similar. The shapes of the manifolds $\omega(k)$ are described in detail by Juniper (2006) for the planar case. The round manifolds have the same topology, although the branch points have different positions along the k_i-axis.

Figure 6 shows the regions of absolute instability for planar flows (figure 6a, b) and round flows (figure 6c–f) as a function of shear and density ratio. Although there are some similarities between the varicose and $m = 0$ modes and between the sinuous and $m = 1$ modes, as suggested by the manifolds, there are also clear differences.

In the planar plug flow case, the dispersion relation is symmetric under the transformation (sinuous, $1/\Lambda, S$) $\leftrightarrow$ (varicose, $-1/\Lambda, S$). Consequently, the regions of parameter space in which the $s2_a$ saddle has positive growth rate are symmetric under this transformation. This saddle, however, does not always lie on the integration path. Consequently, the regions that are absolutely unstable to the $s2_a$ saddle are not symmetric, owing to the saddle selection criteria imposed by the $s1$ saddle, which corresponds to the non-symmetric shear layer. This symmetry of the $s2_a$ saddle in the planar plug flow case does not carry over into the round plug flow case. On the one hand, the $s2_a$ saddle of the round $m = 0$ mode (figure 6c) is absolutely unstable over

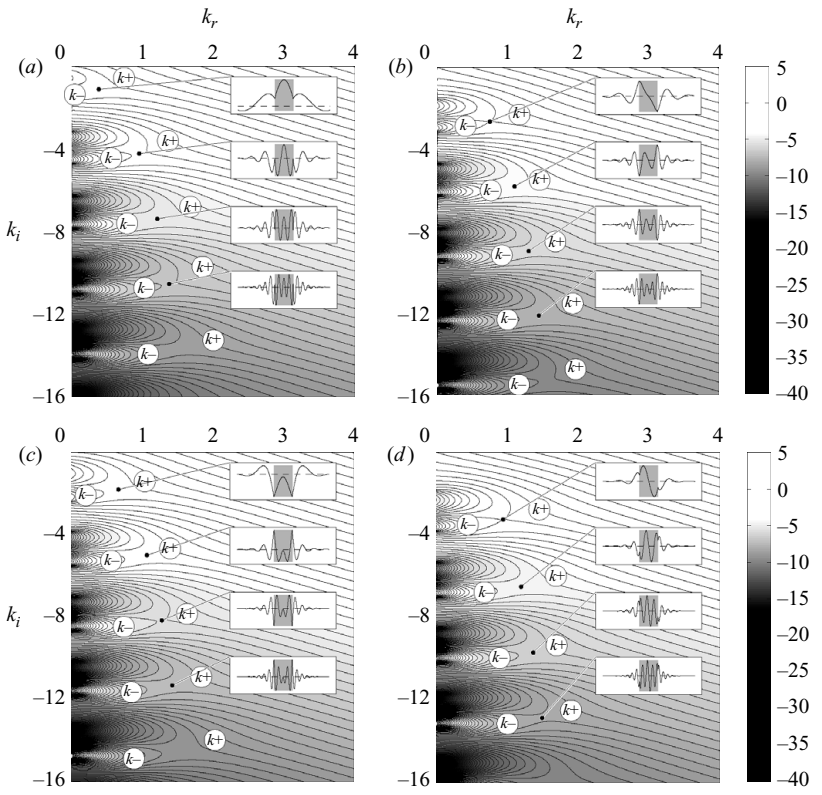

FIGURE 5. Contours of $\omega_i(k)$ for uniform density unconfined wake flows with $(\Lambda, S) = (1, 1)$, showing the $s2$ saddles. The configurations are: (*a*) planar varicose (*b*) planar sinuous (*c*) $m = 0$ (*d*) $m = 1$. The mode shapes are shown in the inset figures, in which the shaded region corresponds to the inner flow.

a larger region of parameter space than that of the planar varicose mode (figure 6*a*). On the other hand, the $s2_a$ saddle of the round $m = 1$ mode (figure 6*d*) is absolutely unstable over a smaller region of parameter space than that of the planar sinuous mode (figure 6*b*). This is particularly evident for wake flows at moderately high density ratio, S.

In these configurations, all saddle points except one have $k \sim 1$. The exception is the saddle point that causes absolute instability of the $m = 0$ mode at large $1/\Lambda$, which has a very small wavenumber when $S \ll 1$. The model assumes that the flow varies over an axial length scale much greater than $1/k$. Consequently, this saddle point may not accurately predict the behaviour of real flows at this extreme density ratio. Nevertheless, the model is sufficiently accurate at moderately low density ratios as shown by the fact that self-sustained global modes have been observed in helium jets, where $S = 0.14$ (Sreenivasan *et al.* 1989).

6. Effect of shear and confinement on uniform density round jets and wakes

6.1. *Effect of confinement on the image system and on positions of saddle points*

The image system of the confined round flow is shown in figure 7(*a*). The outer wall is replaced by an image shear layer with radius R_2^2/R_1. The image system gives

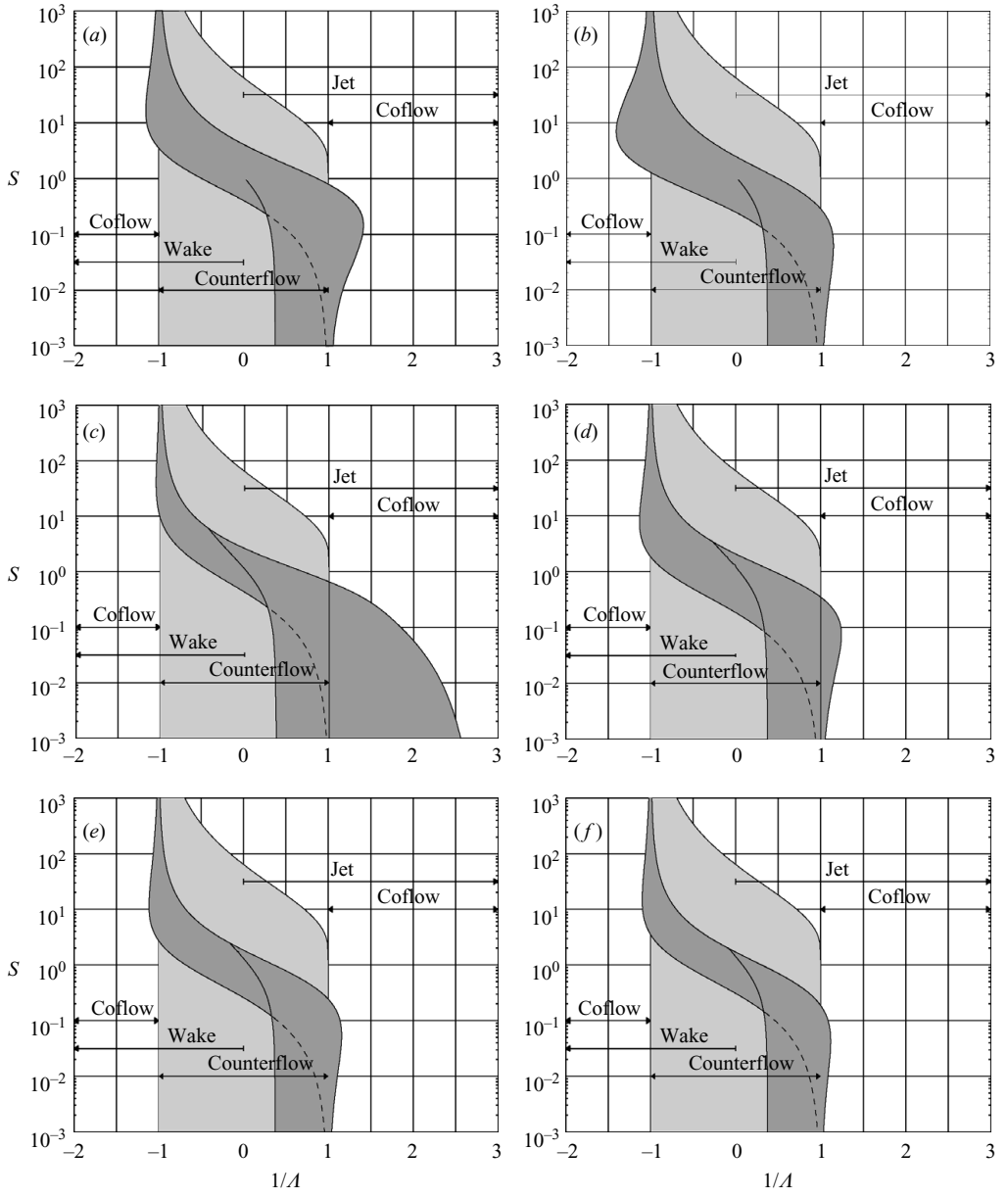

FIGURE 6. Regions of absolute instability for unconfined jets and wakes as a function of shear and density ratio. The configurations are: (*a*) planar varicose, (*b*) planar sinuous, (*c*) $m = 0$, (*d*) $m = 1$, (*e*) $m = 2$ and (*f*) $m = 3$. The absolutely unstable region of the $s1$ saddle is light grey and that of the $s2_a$ saddle is dark grey. The $m = 0$ mode, like the varicose mode, is most unstable to low-density jets. The $m = 1$ mode, like the sinuous mode, is most unstable to high-density wakes. Nevertheless, there are significant differences between the unconfined planar flows and the unconfined round flows.

a useful indication of how the flow will behave at different confinements. At weak confinement (figure 7*b*), the behaviour is similar to that of the unconfined case, as would be expected from the fact that when $\xi R \to \infty$, (2.26) reduces to (2.25). At strong confinement (figure 7*c*) the shear layer and its image become so close that

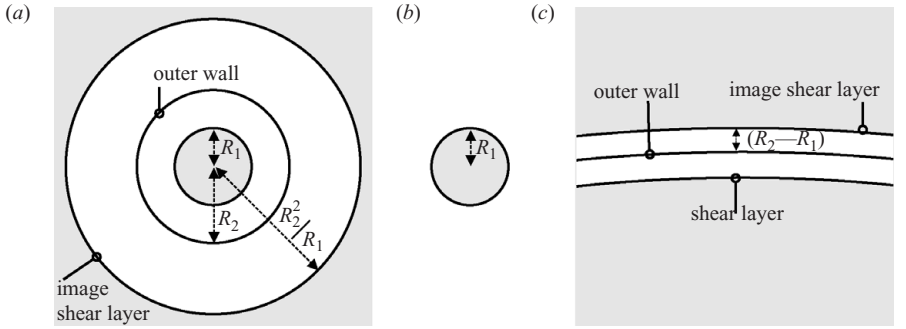

FIGURE 7. The image system of a confined round flow under (*a*) normal confinement, (*b*) weak confinement, when the outer wall is far away and (*c*) strong confinement, when the outer wall is close to the shear layer. The weak confinement case is similar to the unconfined case. The strong confinement case is similar to the planar varicose case with the flows swapped over.

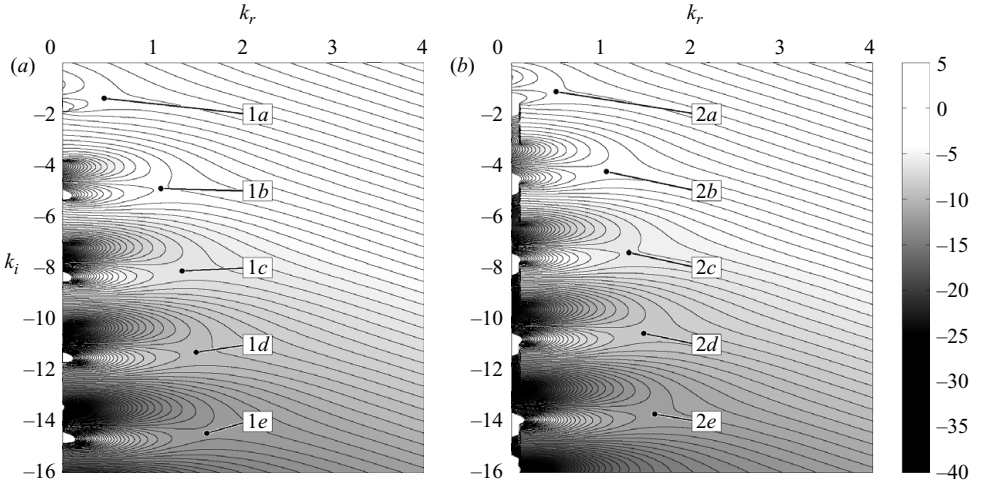

FIGURE 8. (*a*) Contours of $\omega_i(k)$ for the $m = 1$ mode of a uniform density unconfined round wake flow with $(1/\Lambda, S, m) = (-0.9, 1, 1)$. (*b*) Contours of $\omega_i(k)$ for the varicose mode of a uniform density unconfined planar jet flow with $(1/\Lambda, S) = (0.9, 1)$. All saddles are type s_2, as defined in figure 2.

their curvature can be neglected. This means that perturbations with any azimuthal wavenumber, m, behave like varicose perturbations of the planar double shear layer, described in Juniper (2006), under the transformation $U_1 \leftrightarrow U_2$ and reference length scale $h_1 = (R_2 - R_1)$.

The effect of confinement is demonstrated here on the $m = 1$ mode of a flow with $(1/\Lambda, S) = (-0.9, 1)$, which is a counterflow wake with uniform density. At weak confinement, the behaviour is similar to the unconfined round configuration, the saddle points of which are shown in figure 8(*a*). There are $s2$ saddle points at $k_i = -1.38$, -4.90, -8.12, -11.30 and -14.46. For $kr \gg |m^2 - 1/4|$, the Bessel functions that form the mode shape take the form $\exp\{\pm kr\}$. The k_i value therefore represents the wavenumber of oscillations in the r-direction, a feature which is retained qualitatively at lower kr. In this configuration, the characteristic length is the radius of the inner flow, R_1, so these $s2$ saddle points lie at wavenumbers

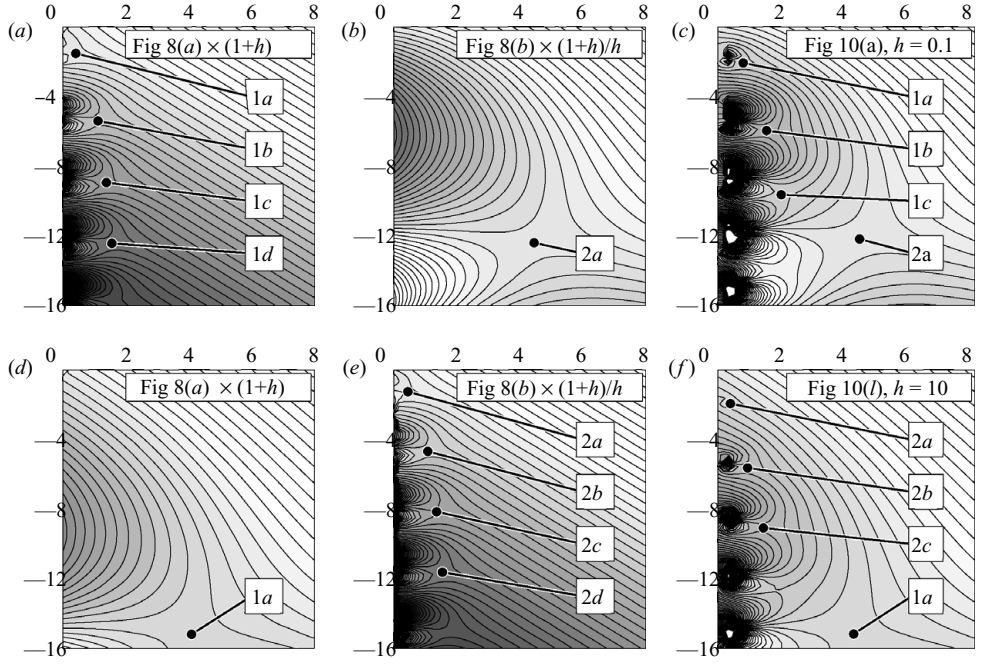

FIGURE 9. Rescaled images of figures 8(*a*) (left) and 8(*b*) (middle), compared with figure 10 (right) in the limit of strong confinement ($h = 0.1$, top frames) and weak confinement ($h = 10$, bottom frames). The features of the unconfined flows in the left and middle frames can be seen to carry through into the confined flows on the right. Intermediate confinements are shown in figure 10.

$k_i = (-1.38, -4.90, -8.12, -11.30, -14.46)/R_1$ in dimensional terms. They represent the zero group velocity modes that scale with the inner flow (labelled 1 in figure 1) and are shown by the dotted lines 1*a*, 1*b* etc. in figure 11(*d*).

At strong confinement, the behaviour is similar to the varicose unconfined planar configuration with the parameters $(-1/\Lambda, 1/S)$, which is shown in figure 8(*b*) as contours of ω_i in the complex k-plane. There are $s2$ saddle points at $k_i = -1.13, -4.25, -7.41, -10.57$ and -13.72. The mode shapes take the form $\exp\{\pm kr\}$, without approximation, so the k_i value also represents the wavenumber of oscillations in the r-direction. In this configuration, the characteristic length is the thickness of the outer fluid, $R_2 - R_1$, so these $s2$ saddle points lie at wavenumbers $k_i = (-1.13, -4.25, -7.41, -10.57, -13.72)/(R_2 - R_1)$ in dimensional terms. They represent the zero group velocity modes that scale with the outer flow (labelled 2 in figure 1) and are shown by the dotted lines 2*a*, 2*b* etc. in figure 11(*d*).

At intermediate confinement, modes with zero group velocity in the inner flow interact with those in the outer flow. This can be seen through the interaction of the saddle points in figure 10, which shows contours of ω_i in the k-plane at twelve values of confinement. The axes of these figures have been multiplied by $(1 + h)$ so that approximately the same number of saddle points appear in each figure.

Figures 9(*a*)–9(*c*) show $\omega_i(k)$ in the strong confinement limit ($h \ll 1$). The $s2$ saddle points that scale with the inner flow, 1*a*, 1*b* and 1*c*, can be identified. Their positions in figure 8(*a*) should be multiplied by $(1 + h) = 1.1$ to obtain their approximate positions in figure 10(*a*). Similarly, an $s2$ saddle point that scales with the outer flow,

$2a$, can be identified. Its position in figure 8(b) should be multiplied by $(1+h)/h = 11$ to obtain its approximate position in figure 10(a). At strong confinement, the highest value of ω_i is held by saddle $2a$, which is the fundamental mode of the outer flow.

Figures 9(d)–9(f) show $\omega_i(k)$ in the weak confinement limit ($h \gg 1$). The $s2$ saddle points that scale with the outer flow, $2a$, $2b$ and $2c$ can be identified. Their positions in figure 8(b) should be multiplied by $(1 + h)/h = 1.1$ to obtain their approximate positions in figure 10(l). Similarly, an $s2$ saddle point that scales with the inner flow, $1a$, can be identified. Its position in figure 8(a) should be multiplied by $(1 + h) = 11$ to obtain its approximate position in figure 10(l). At weak confinement, the highest value of ω_i is held by saddle $1a$, which is the fundamental mode of the inner flow.

At intermediate confinement ($h \sim 1$), there is strong interaction between the inner and outer flows. As h increases from 0.1 to 10, the saddle point with highest ω_i swaps from the fundamental mode of the outer flow, $2a$, to the fundamental mode of the inner flow, $1a$, via two saddle points with particularly high ω_i, labelled $c1$ and $c2$. These combined modes arise owing resonance between the inner and outer flows.

6.2. *Physical interpretation of the effect of confinement*

The k_i values of the saddle points in figure 10 are shown as solid lines in figure 11(d) as a function of h. At each value of h, the saddle point with the highest growth rate, ω_i, is shown as a bold line whose thickness increases with ω_i. The dotted lines are the k_i values of the saddle points that scale with the inner and outer flows when uncombined, as described at the start of §6.1. The combined flow is most unstable when the solid line is close to the intersection of two dotted lines. This is at values of h where the k_i value of the combined mode is close to the k_i value of a mode in the inner flow and a mode in the outer flow. At these points, the interaction between the inner and outer flows is strongly constructive. Conversely, the flow is more stable at intermediate values of h, where the k_i values of the inner modes lie between those of the outer modes.

This explains the features on the left of the map of absolute instability in the $(1/\Lambda, S)$ plane shown in figure 12(d). The regions that are absolutely unstable to the $s2$ saddle points are shown in dark grey. Confinement, h, affects the amount of shear that is required for the $s2$ saddles to be absolutely unstable. When h is such that the modes with zero group velocity in the inner and outer flows have similar wavenumbers in the r-direction, less shear is required for absolute instability because there is constructive interference between the modes in each flow. This occurs, for example, around $h = 0.8$ for the $m = 1$ case. The region that is absolutely unstable to the $s1$ saddle is shown in light grey.

The $m = 0$, $m = 2$ and $m = 3$ modes have been analysed in the same way and the results are shown in the other frames of figures 11 and 12. They have the same features as the $m = 1$ mode. The planar results are shown for comparison. The behaviour of the confined $m = 0$ mode is similar to the confined planar varicose case and the behaviour of the confined $m = 1$ mode is similar to the confined planar sinuous case. The modes at higher m are always more stable, except for a small region around $(1/\Lambda, h) = (-1, 0.3)$, where the $m = 2$ mode is most unstable.

6.3. *Saddle points that cross the k_i-axis*

The dark grey regions of figures 6 and 12 correspond to absolute instability of the $s2$ saddles in the unconfined and confined situations. When weakly confined (e.g. figure 12(c) with $h = 10$), the dark grey region extends over a larger range of shear than in the corresponding unconfined case (figure 6(c) with $S = 1$). This is due to

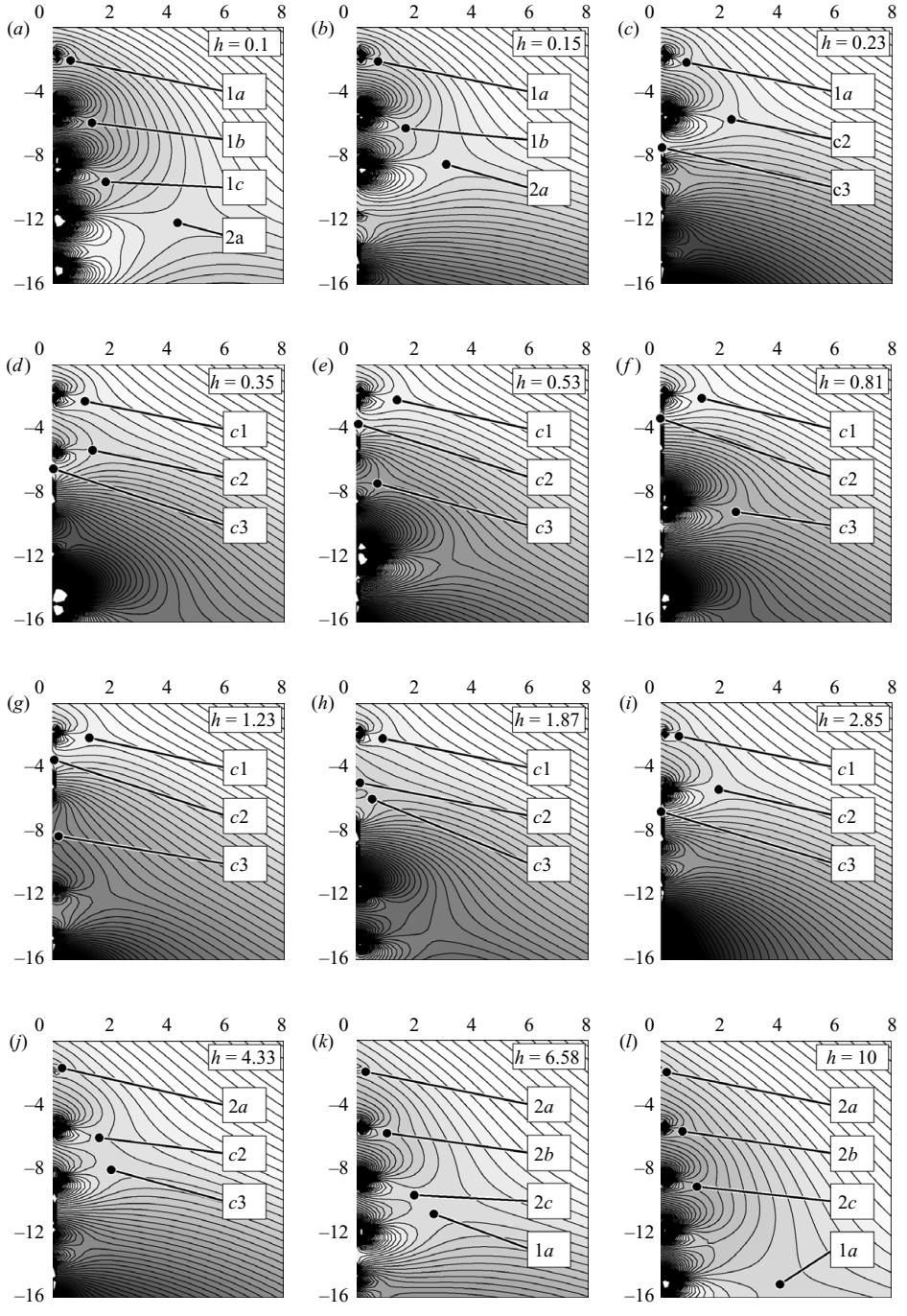

FIGURE 10. Contours of $\omega_i(k)$ for the $m = 1$ mode of a confined wake flow with $(1/\Lambda, S, m) = (-0.9, 1, 1)$. Horizontal axis: $k_r(1 + h)$. Vertical axis: $k_i(1 + h)$. At strong confinement (small h), the saddle points that correspond to the inner flow ($1a$ to $1c$) are bunched around the k_i-axis and the highest saddle point corresponds to the outer flow ($2a$). At weak confinement (large h), the saddle points that correspond to the outer flow ($2a$ to $2c$) are bunched around the k_i-axis and the highest saddle point corresponds to the inner flow ($1a$). At intermediate confinement, there is strong interaction between the inner and outer flows, which produces combined modes ($c1$, $c2$) that have particularly high growth rates.

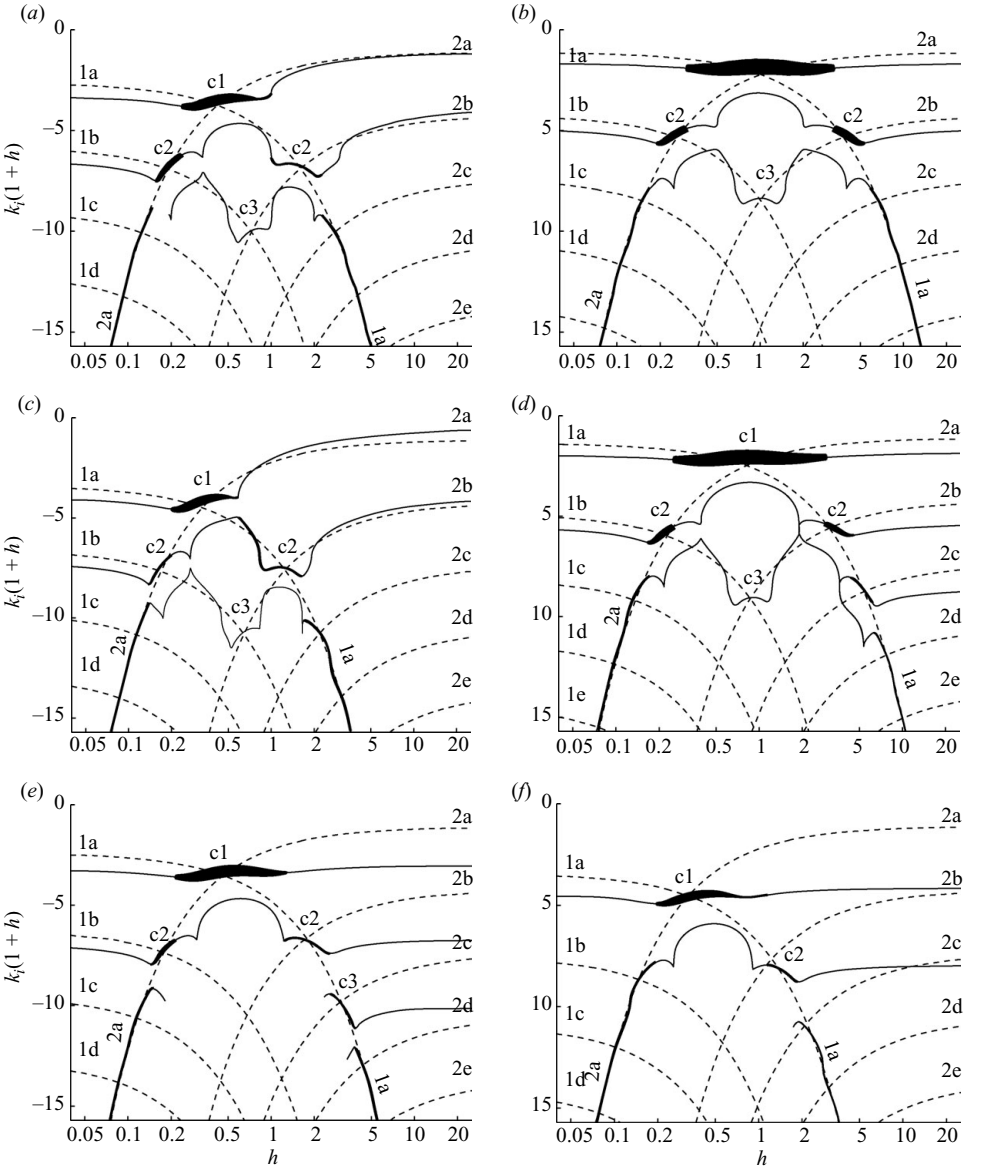

FIGURE 11. Solid lines: the radial wavenumbers, k_i, of the significant saddle points of confined wake flows with $(1/\Lambda, S) = (-1, 1)$. The line thickness increases with the absolute growth rate ω_i and has the same scale on all figures. Dotted lines: the radial wavenumbers of the saddle points in the inner flow, $1a, 1b, \ldots$, and the outer flow, $2a, 2b, \ldots$. The figures represent (*a*) varicose, (*b*) sinuous, (*c*) $m = 0$, (*d*) $m = 1$, (*e*) $m = 2$ and (*f*) $m = 3$. The flows have higher absolute growth rates at values of h when the saddle points (i.e. modes with zero group velocity) in the inner and outer flows have the same radial wavenumber, which is at the intersections of the dotted lines.

subdominant $s2$ saddles crossing the k_i-axis in the unconfined case, as summarized here. Full details can be found in Healey (2007) and Juniper (2007).

At some parameter values in the unconfined case, an $s2$ saddle point on the integration path crosses the k_i-axis into the plane of diverging eigenfunctions, as described

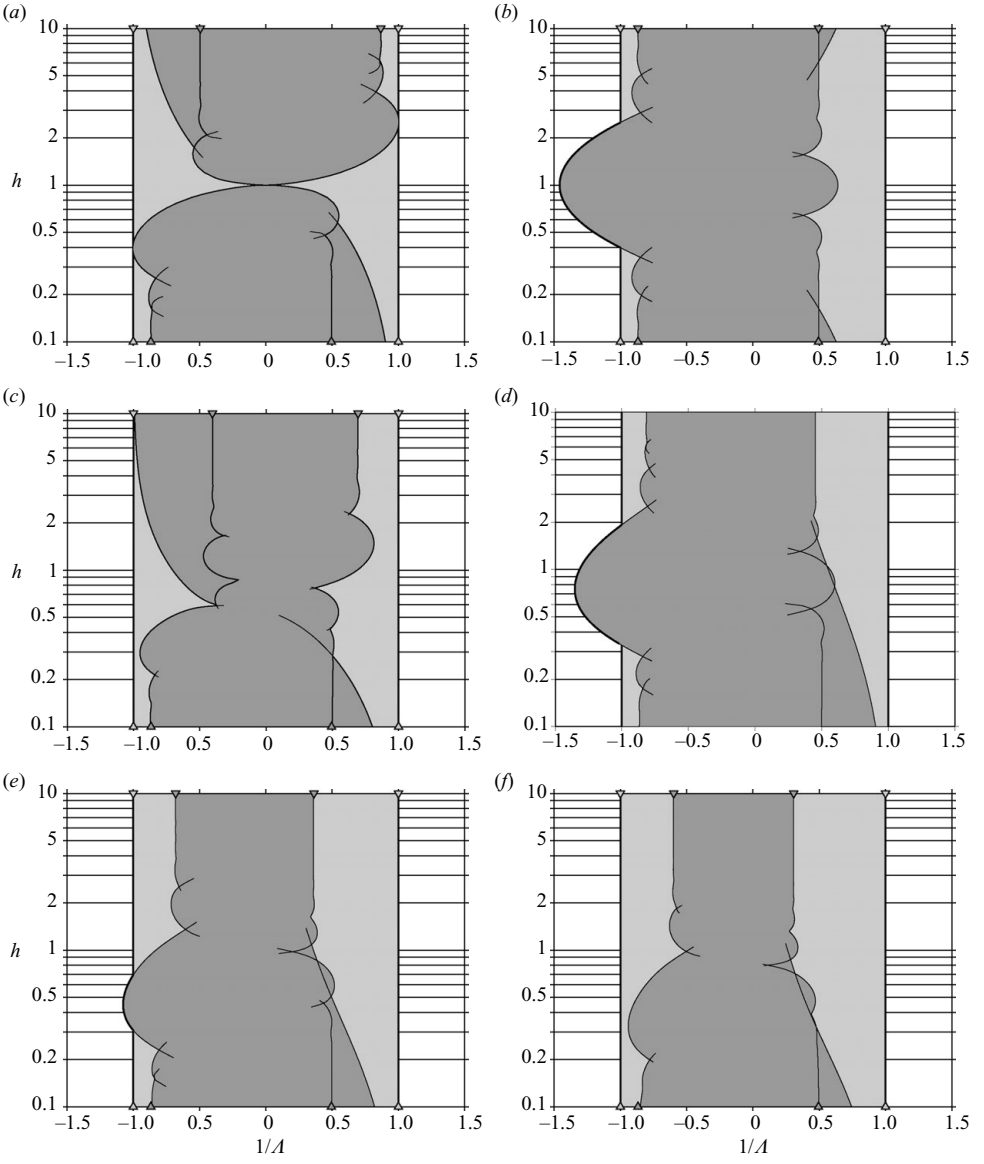

FIGURE 12. Regions of absolute instability as a function of shear and confinement for uniform density jets and wakes. The configurations are: (*a*) varicose, (*b*) sinuous, (*c*) $m = 0$, (*d*) $m = 1$, (*e*) $m = 2$ and (*f*) $m = 3$. The absolutely unstable region of the $s1$ saddle is light grey and that of the $s2$ saddles is dark grey. The triangular markers correspond to the unconfined and strongly confined limits. Despite the difference between the unconfined cases (figure 6), the $m = 0$ mode behaves similarly to the varicose mode, and the $m = 1$ mode behaves similarly to the $m = 1$ mode when the confinement is varied. (*b*) is a corrected version of figure 16(*e*) of Juniper (2007): the dark grey region at $h = 1$ extends only to $1/\Lambda = 0.62$, and the contributions from all the subdominant $s2$ saddles have been included.

in § 2.6 (see figure 7 of Juniper (2007) for an example). There can be situations in which the k^+ branch of this saddle point has positive growth rate when it crosses the k_i-axis, even though the saddle itself has negative growth rate. In the confined case, saddle points cannot cross the k_i-axis, so in these situations the k^+ branch

pinches with a series of saddle points that have positive growth rate and sit just to the right of the k_i-axis. The top saddle point in the confined case has positive growth rate, even though the saddle point in the corresponding unconfined situation has negative growth rate. When this is the dominant saddle point (the highest on the integration path), this causes the flow to be absolutely unstable when weakly confined, even though it is convectively unstable when unconfined. Physically, this arises because, in these situations, parts of the wavepacket contain eigenfunctions that grow in the radial direction, even though the wavepacket is decaying at the point of impulse. When unconfined, these parts of the wavepacket can propagate away to infinite radius without affecting the point of impulse. When confined, however, they reflect off the confining wall and return to the point of impulse, eventually setting up a standing wave that grows at the point of impulse and therefore makes the flow absolutely unstable in the long-time limit.

In non-swirling round jets and wakes, this situation arises only in counterflow, in which the s_1 saddle is already absolutely unstable and dominant. This means that the s_2 saddles that cross the k_i-axis, and their counterparts in the confined case, are always subdominant and therefore that they do not enlarge the region of parameter space that is absolutely unstable. They do, however, enlarge the region of parameter space that is absolutely unstable to the $s2$ saddles. This is why the dark grey region of the round weakly confined case is larger than that of the corresponding unconfined case.

In this respect, round jets and wakes behave differently from planar jets and wakes. In the planar case, $s2$ saddles that cross the k_i-axis can be dominant. This means that the entire absolutely unstable region of the weakly confined planar case (not just the region due to the $s2$ saddles) is larger than that of the corresponding unconfined case.

7. Effect of density ratio, shear and confinement

The analysis in §6 has been repeated at different density ratios. Figure 13 shows the absolutely unstable region of $(1/\Lambda, h)$-space at seven values of S for the round $m = 0$ mode. The light grey region is absolutely unstable to the $s1$ saddle and the dark grey region is absolutely unstable to the $s2$ saddles. This can be compared directly with figure 15 of Juniper (2006), which shows the same plots for the $s2$ saddles of the planar varicose mode.

With the exception of $S = 0.001$, the plots for the confined $m = 0$ mode are very similar to those of the confined planar varicose mode, despite the differences that exist when unconfined. The plots are identical for $h \ll 1$ because the round case tends towards the planar case in this limit, as described in §6. Confinement enhances the transition to absolute instability at some values of h, but inhibits this transition at other values of h. The latter effect is less pronounced in the round case than in the planar case. At low density ratios, the unconfined round $m = 0$ mode is more unstable than the unconfined planar varicose mode. This effect carries over into the confined case and is clearly related more to the density ratio than to the confinement.

When $S = 0.001$, the dark grey region at $1/\Lambda < 1$ is bounded by the envelope of several $s2$ saddles, not by the single $s2$ saddle that is seen in the equivalent figure of the planar case in Juniper (2006). If the planar model had included a stabilization mechanism, the same effect would have been seen in that figure. Hence, at $S = 0.001$ as at other density ratios, the behaviour of the round $m = 0$ mode is similar to that of the planar varicose mode.

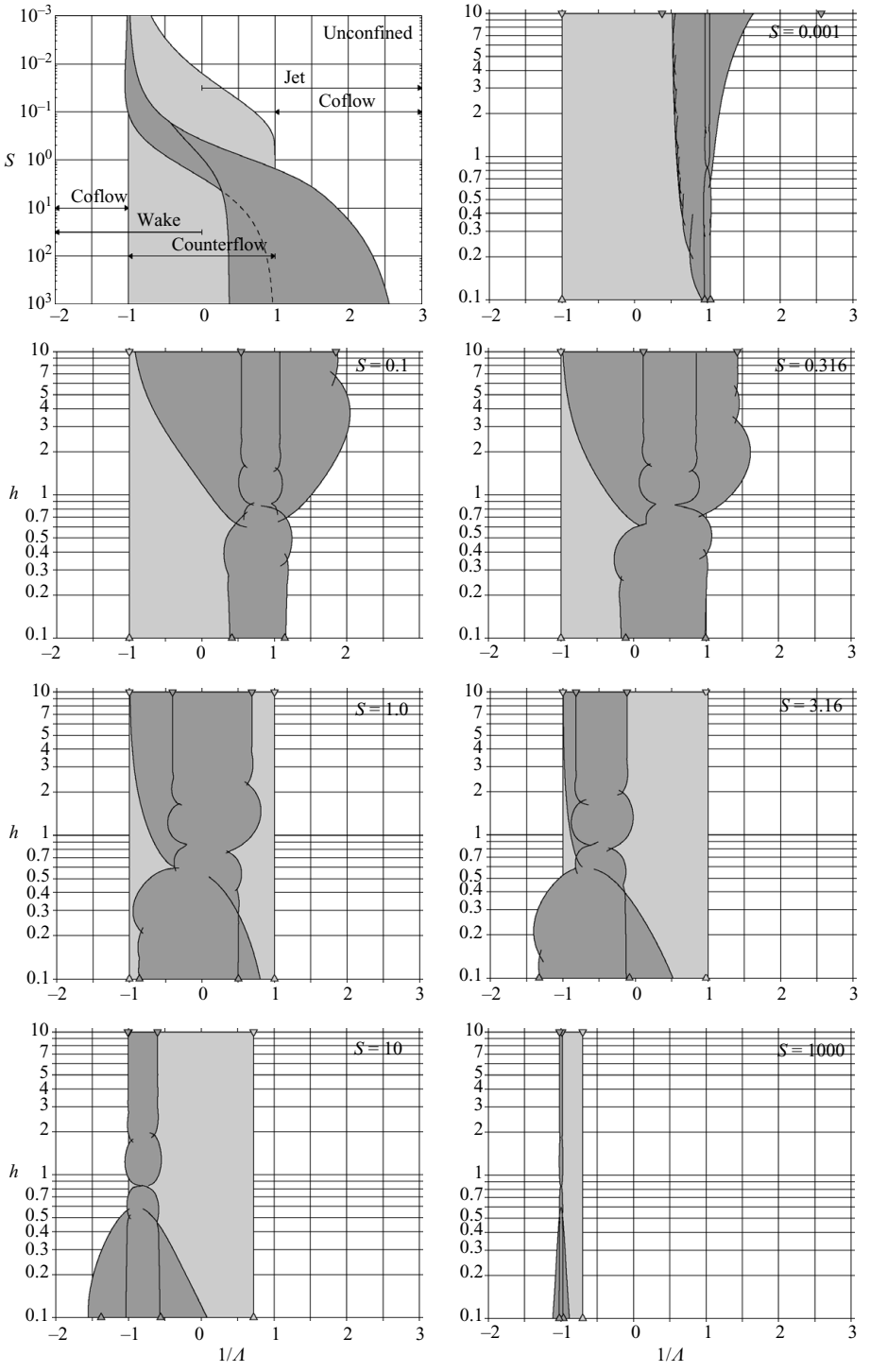

FIGURE 13. Regions of absolute instability for the $m = 0$ mode of confined jets and wakes as a function of shear, density ratio and confinement. The absolutely unstable region of the $s1$ saddle is light grey and that of the $s2$ saddles is dark grey. The top left figure is the unconfined case and the remaining figures are in the $(1/\Lambda, h)$-plane at different density ratios. This figure can be compared directly with figure 15 of Juniper (2006).

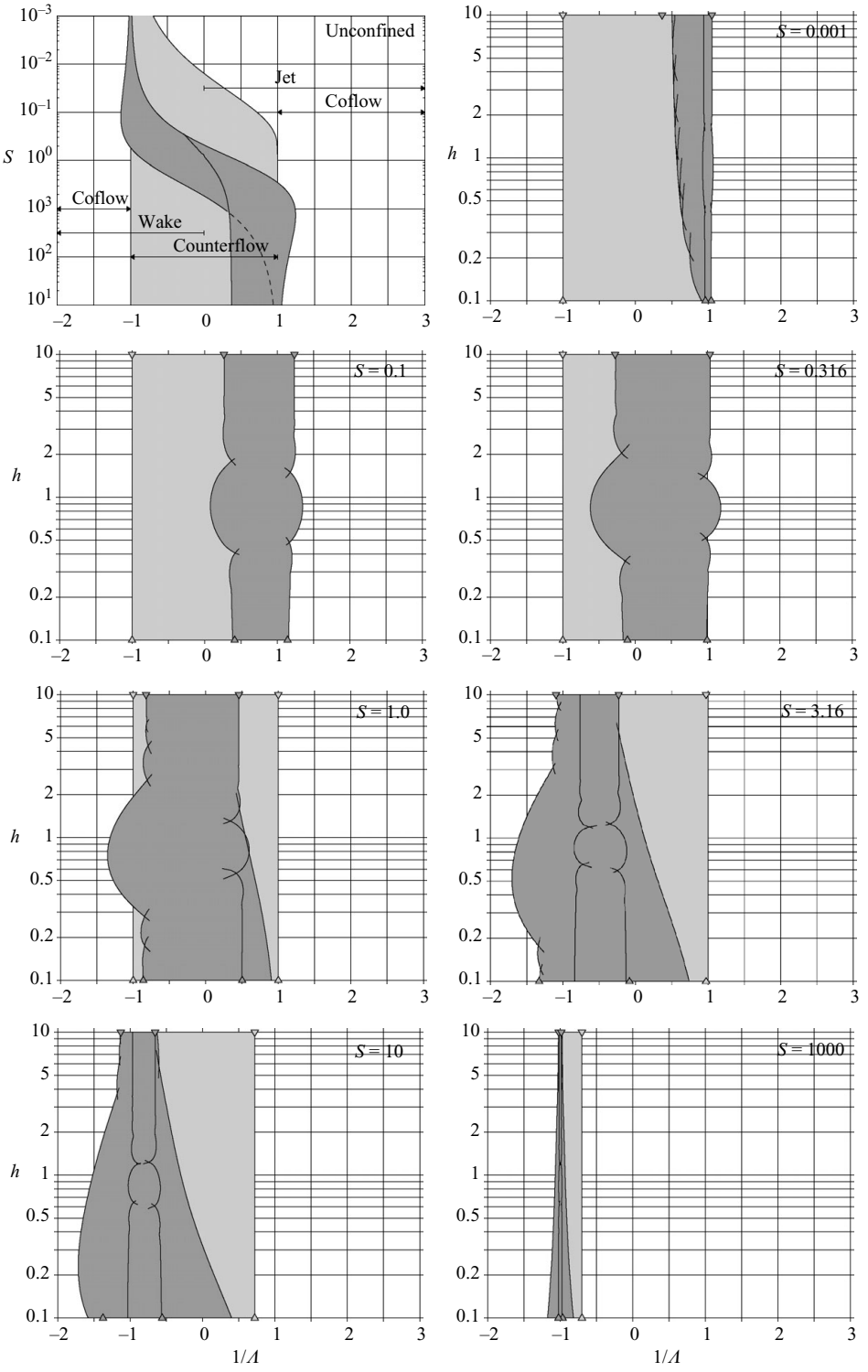

FIGURE 14. As for figure 13 but for the $m = 1$ mode, which can be compared with figure 16 of Juniper (2006).

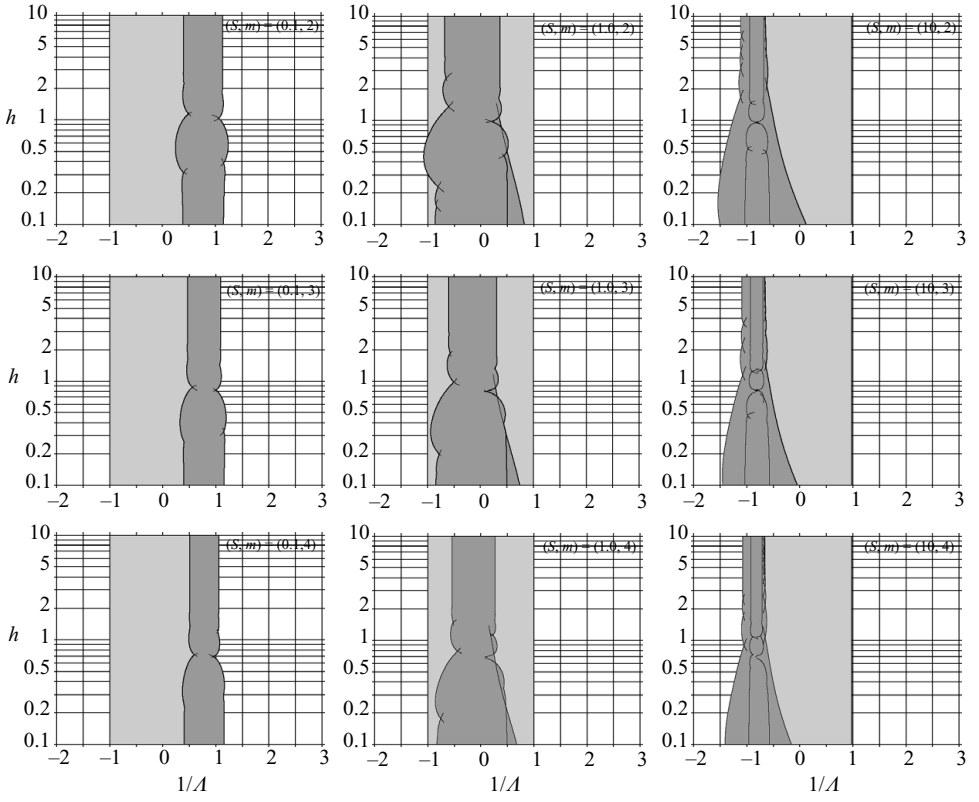

FIGURE 15. As for figure 13 but for the $m = 2$, $m = 3$ and $m = 4$ modes at three density ratios.

Figure 14 shows the same plots for the round $m = 1$ mode. This can be compared with figure 16 of Juniper (2006), which shows the planar sinuous mode. The effect of confinement on the $m = 1$ mode is similar to that on the sinuous mode. At high density ratios, the unconfined $m = 1$ mode is more stable than the unconfined sinuous mode. This effect also carries over into the confined case.

Figure 15 shows the effect of confinement on the round $m = 2$, $m = 3$ and $m = 4$ modes. It is qualitatively identical to its effect on the $m = 0$ and $m = 1$ modes. There is little further comment to make on these modes, except that the $m \geqslant 2$ modes are almost always more stable than the $m = 0$ and $m = 1$ modes.

8. Conclusions

In this paper, the effect of confinement has been investigated on the convective/absolute transition of non-swirling round jet/wake flows. Two model flows are examined, one with a piece-wise linear radial velocity profile and one with a plug flow profile. Both models are inviscid and incompressible. A spatio-temporal stability analysis is performed on both models while varying the following parameters: shear number, density ratio, confinement and the azimuthal wavenumber. In the limit of large axial wavenumber, the dispersion relation of the plug flow model tends to that of the equivalent planar jet/wake flow.

The long-time response is calculated in the entire outer fluid, rather than just at the point of impulse. The $s1$ saddle points, which are associated with the shear layer, are distinguished from the $s2$ saddles, which are associated with the jet/wake motion. When the shear layer is thin, the $s1$ saddle has the same behaviour in all flows. The $s2$ saddles are the main focus of this paper because their behaviour differs between the different types of jet/wake flows.

In the planar jets and wakes studied by Juniper (2007), this approach revealed that, at certain parameter values, parts of the back of the wavepacket can grow upstream even though the response decays at the point of impulse. This occurs if a dominant $s2$ saddle point (i.e. the highest saddle on the integration path) crosses the k_i-axis and has both negative growth rate and a k^+ branch that has positive growth rate where it intersects the k_i-axis. This causes some flows that are convectively unstable when unconfined to become absolutely unstable when weakly confined. In the round case, this behaviour is only seen when the $s1$ saddle is already dominant. The $s2$ saddles that cross the k_i-axis are always subdominant and, consequently, round flows that are convectively unstable when unconfined always remain convectively unstable when confined.

In terms of its motion, the round $m = 0$ mode is analogous to the planar varicose mode and the round $m = 1$ mode is analogous to the planar sinuous mode. When unconfined, the $s2$ saddles of the planar varicose mode have the same instability behaviour as those of the planar sinuous mode under the transformation $(1/\Lambda, S) \leftrightarrow (-1/\Lambda, 1/S)$. In other words, the $s2$ saddles of the two modes are equally unstable, although in different regions of parameter space. The unconfined round $m = 0$ mode, however, is absolutely unstable over a larger region of parameter space than the planar varicose mode. In contrast, the unconfined round $m = 1$ mode is absolutely unstable over a smaller region of parameter space than the planar sinuous mode, particularly for dense wakes. There are significant differences between the unconfined round case and the unconfined planar case and there is no equivalence between the $m = 0$ mode and the $m = 1$ mode.

Nevertheless, the effect of confinement on the round $m = 0$ mode is very similar to the effect of confinement on the planar varicose mode, despite the differences that exist between the two modes when unconfined. Similarly, the effect of confinement on the round $m = 1$ mode is very similar to the effect on the planar sinuous mode. The effect of confinement on higher-order round modes is similar, but these modes are almost always more stable than the $m = 0$ and $m = 1$ modes.

When weakly confined, the long-time behaviour of round flows is dominated by the normal modes with zero group velocity that are in the inner fluid. When strongly confined, the long-time behaviour of the round flows is dominated by the normal modes with zero group velocity that are in the outer fluid. At intermediate confinements, the modes with zero group velocity that are in the inner fluid interact with those that are in the outer fluid. This can be observed through the interaction of saddle points in the wavenumber plane. Flows are particularly unstable when these modes' wavenumbers in the radial direction match. Flows are more stable when their wavenumbers are far apart. This behaviour is the same as that seen in planar jet/wake flows.

Confined shear injectors are consistently used in industrial injection systems that require good mixing with a low pressure drop. It is likely that this is because they stimulate an unstable global shear mode whose large-scale bulging ($m = 0$), spiralling ($m = 1$) or flapping (combined $m = 1$ and $m = -1$) motion enhances mixing. This paper confirms that unconfined light jet flows are more unstable than unconfined

dense wake flows. It goes on to show that, for both types of flow, confinement can increase or decrease their instability, depending on the value of the confinement parameter. This paper presents useful design rules for such injectors, such as the optimum confinement for a given density ratio.

REFERENCES

Bearman, P. & Zdravkovich, M. 1978 Flow around a circular cylinder near a plane boundary. *J. Fluid Mech.* **89**, 33–47.

Delbende, I. & Chomaz, J.-M. 1998 Nonlinear convective/absolute instabilities in parallel planar wakes. *Phys. Fluids* **10**(11), 2724–2736.

Huerre, P. 2000 Open shear flow instabilities. In *Perspectives in fluid dynamics – A Collective Introduction to Current Research* (ed. G. K. Batchelor, H. K. Moffat & M. G. Worster). Cambridge University Press.

Huerre, P. & Monkewitz, P. 1990 Local and global instabilities in spatially developing flows. *Ann. Rev. Fluid Mech.* **22**, 473–537.

Healey, J. 2006 A new convective instability of the rotating-disk boundary layer with growth normal to the plate. *J. Fluid Mech.* **560**, 279–310.

Healey, J. 2007 Enhancing the absolute instability of a boundary layer by adding a far-away plate. *J. Fluid Mech.* **579**, 29–61.

Juniper, M. 2006 The effect of confinement on the stability of planar shear flows. *J. Fluid Mech.* **565**, 171–195.

Juniper, M. 2007 The full impulse response of two-dimensional jet/wake flows and implications for confinement. *J. Fluid Mech.* **590**, 163–185.

Juniper, M. & Candel, S. 2003 The stability of ducted compound flows and consequences for the geometry of coaxial injectors. *J. Fluid Mech.* **482**, 257–269.

Monkewitz, P. & Sohn, K. 1988 Absolute instability in hot jets. *AIAA J.* **26**, 911–916.

Shair, F. & Grove, A. & Petersen, E. & Acrivos, A. 1963 The effect of confining walls on the stability of the steady wake behind a circular cylinder. *J. Fluid Mech.* **17**, 546–550.

Sreenivasan, K. & Raghu, S. & Kyle, D. 1989 Absolute instability in variable density round jets. *Exps. Fluids* **7**, 309–317.

Yu, M.-H. & Monkewitz, P. 1990 The effect of nonuniform density on the absolute instability of planar inertial jets and wakes. *Phys. Fluids* A **2**(7), 1175–1181.